

# Spectral fluctuations and crossovers in multilayer network

Himanshu Shekhar<sup>1\*</sup>, Ashutosh Dheer<sup>1</sup>, Santosh Kumar<sup>1</sup>, N. Sukumar<sup>2</sup>

<sup>1</sup>*Department of Physics, Shiv Nadar Institution of Eminence, Gautam Buddha Nagar, UP, India, 201314 and*

<sup>2</sup>*Amrita School of Artificial Intelligence, Amrita Vishwa Vidyapeetham, Coimbatore, 641112, Tamil Nadu, India.\**

(Dated: August 19, 2025)

We investigate spectral fluctuations in multilayer networks within the random matrix theory (RMT) framework to characterize universal and non-universal features. The adjacency matrix of a multilayer network exhibits a block structure, with diagonal blocks representing intra-layer connections and off-diagonal blocks encoding inter-layer connections. Applying appropriate scaling factors for these blocks, we equalize variances across inter- and intra-layers, enabling direct comparison of spectral statistics. We analyze eigenvalue spectra across multilayer network configurations with varying inter- and intra-layer connectivities. Introducing a crossover model for bilayer networks, we capture the smooth transition of spectral properties from block-diagonal (two independent GOEs) to single-layer (one GOE) statistics as the relative strength of inter-layer to intra-layer connection varies. Furthermore, we analyze interatomic distance networks derived from protein crystal structures, including 1EWT, 1EWK, and 1UW6, to demonstrate applicability. Our findings reveal that the universality of spectral fluctuations persists across multilayer network architectures and highlight RMT as a robust tool for probing topological and dynamical complexities of real-world networks.

## I. INTRODUCTION

Complex systems permeate the natural and engineered world, from neural circuits and social dynamics to infrastructural grids and biological assemblies [1–5]. Understanding such systems requires modeling the interactions among their constituent elements, often using tools from network science. At its core, a network is an abstraction: nodes represent entities, and edges represent interactions or relationships between these entities. This abstraction allows a systematic comparison of otherwise disparate systems.

This formalization underpins graph theory, which originated with Euler’s solution [6] to the Seven Bridges of Königsberg problem in 1736. Over time, graph theory has evolved into a powerful mathematical and computational framework for analyzing connectivity, structure, and dynamics in complex systems, driven by applications in sociology, epidemiology, computer science, physics, economics, and molecular biology [7–15]. Foundational models such as the Erdős-Rényi (ER) random graph, the Watts-Strogatz small-world network, and the Barabási-Albert scale-free network have provided benchmarks for understanding how topology influences robustness, diffusion, synchronization, and percolation [16–21].

Mathematically, the structure of a network is encoded in its adjacency matrix, a square matrix whose entries specify the presence or weight of edges. For undirected simple graphs, the adjacency matrix is a symmetric matrix with eigenvalues that are real-valued. Spectral graph theory relates these eigenvalues and their eigenvectors to network properties such as connectivity, community structure, and diffusion dynamics. Beyond such struc-

tural measures, the statistical fluctuations of eigenvalues reveal the system’s degree of order or randomness. In this context, random matrix theory (RMT) becomes remarkably useful as a statistical framework for characterizing spectral fluctuations in complex networks. RMT posits that large, complex systems exhibit universal spectral fluctuation statistics determined only by symmetry class, regardless of microscopic details. For adjacency matrices of large random graphs, the nearest-neighbor spacing distribution (NNSD) of eigenvalues follows the Wigner-Dyson distribution [22, 23] characteristic of the Gaussian ensembles in RMT. The spacing ratio distribution (SRD), which avoids spectral unfolding, captures the same universal features and is particularly robust for empirical and finite-size networks. A vast number of real-world applications of network analysis through RMT have been documented across diverse domains [24–27].

However, many real-world systems are inherently multilayered, where nodes interact through multiple types of connections or participate in various contexts simultaneously. Examples include multimodal transportation systems, multiplex social networks, interconnected infrastructure grids, and biological systems such as interatomic distance networks in proteins. Modeling such systems as single-layer networks can obscure essential structural correlations, differences in layer structure, and the interplay between intra-layer and inter-layer connectivity. In the multilayer network formalism [28–30], the adjacency matrix acquires a block structure: diagonal blocks encode intra-layer connections, and off-diagonal blocks encode inter-layer connections. This richer representation allows a more faithful description of real systems but also raises new questions: How do spectral fluctuations behave in multilayered networks? Can they display features akin to the universal signatures predicted by RMT?

Spectral analysis of multilayer networks has begun to attract attention [31–35], particularly in multiplex con-

\* <sup>1</sup>himanshuphy02@gmail.com, ad326@snu.edu.in, Deceased, <sup>2</sup> n.sukumar@cb.amrita.edu

figurations where the same set of nodes is present in each layer. Yet, a systematic exploration of universality in general multilayer architectures—those with differing sizes, connection probabilities, and intra-/inter-layer structures—remains limited. Moreover, recovering RMT universality in such systems requires careful treatment: without appropriate scaling, block variances may differ substantially, leading to spurious deviations from universal statistics.

In this work, we develop a general RMT-based framework for spectral fluctuation analysis in multilayer networks. We treat the most general architectures, including networks with only intra-layer connections, only inter-layer connections, both types, and multiplex structures. To ensure comparability of spectral fluctuations across layers, we introduce scaling factors for diagonal and off-diagonal blocks that normalize variances irrespective of block size or connection probability. Fluctuations are characterized using higher-order spacing ratios, which are sensitive to spectral correlations and avoid the need for unfolding.

Our analysis proceeds in two parts. First, we construct ensembles of random multilayer networks with ER connectivity and systematically vary intra-layer and inter-layer connection probabilities to explore the dependence of spectral statistics on connectivity patterns. This is then generalized by introducing a crossover model for bilayer networks, in which the relative strength of intra-layer and inter-layer couplings is tuned to track the transition from two independent GOEs to a single GOE. Second, we apply the framework to empirical multilayer networks derived from protein crystal structures (1EWT, 1EWK, and 1UW6), modeling residues as nodes and spatial proximity as edges. By varying distance thresholds, we probe how changes in intra- and inter-layer connectivity drive transitions between universality classes, using both SRD and cumulative SRD (CSR) to quantify the behavior. We find that with appropriate scaling, multilayer networks exhibit the universal spectral fluctuations predicted by RMT, even in the presence of structurally distinct layers and varying topologies. These results establish a general framework for quantifying spectral universality and inter-layer coupling in layered systems, with applications from communication and transportation networks to complex biological assemblies.

The paper is organized as follows. In section II we define the multilayer network model, its adjacency matrix representation, and the scaling procedure required to recover universal spectral fluctuations. Section III presents the spectral statistics of random multilayer networks for different architectures, including the bilayer crossover model. In section IV we apply the framework to empirical multilayer networks derived from protein crystal structures, and summarize the results and discuss possible extensions in section V.

## II. PRELIMINARIES

### A. Multilayer Network and General Matrix Model

A multilayer network can be defined as a function  $\Phi \equiv \Phi(G, E)$  of two sets: a set of graphs  $G$  and a set  $E$  of connections. The set  $G = \{g_a | a = 1, 2, \dots, m\}$  is the set of graphs in each layer, where each graph  $g_a \equiv g_a(N_a, e_a)$  is defined by the set of nodes  $N_a$  and the set of edges  $e_a$ . The set  $E = \{e_{ab} | a, b \in \{1, 2, \dots, m\}\}$  contains connections between nodes; elements of  $E$  could denote intra-layer connections (if  $a = b$ ), or inter-layer connections (if  $a \neq b$ ) between nodes  $N_a$  and  $N_b$  of layers  $g_a$  and  $g_b$  [29, 33].

Networks can be represented by adjacency matrices which for multilayered networks take the form of block-structured matrices. Considering an undirected network structure, an  $m$ -layer network with each layer having, in general, a different number of nodes  $(n_1, n_2, \dots, n_m)$  can be represented by the following adjacency matrix

$$\mathcal{A} = \begin{bmatrix} A_{n_1 \times n_1}^1 & B_{n_1 \times n_2}^{1,2} & \dots & B_{n_1 \times n_m}^{1,m} \\ (B^{1,2})_{n_2 \times n_1}^T & A_{n_2 \times n_2}^2 & \dots & B_{n_2 \times n_m}^{2,m} \\ \vdots & \vdots & \ddots & \vdots \\ (B^{1,m})_{n_m \times n_1}^T & (B^{2,m})_{n_m \times n_2}^T & \dots & A_{n_m \times n_m}^m \end{bmatrix}. \quad (1)$$

The  $j$ th diagonal block,  $A_{n_j \times n_j}^j$ , is the adjacency matrix of the  $j$ th layer and is of size  $n_j \times n_j$ . Its off-diagonal entries carry information about the associated intra-layer connections and its diagonal elements are all zero. Hence, within the unweighted network setup, if  $a_{xy}^k$  is an element of  $A_{n_k \times n_k}^k$ , then  $a_{xy}^k = 0$  implies that nodes  $x$  and  $y$  in the  $k$ th layer, are not connected, whereas  $a_{xy}^k = 1$  means that they are connected.  $B_{n_j \times n_k}^{j,k}$  are off-diagonal blocks of size  $n_j \times n_k$  and represents the intra-layer connection between layers  $j$  and  $k$ . If  $b_{xy}^{k,l}$  is an element of  $B_{n_k \times n_l}^{k,l}$ , then  $b_{xy}^{k,l} = 0$  means that the node  $x$  of the  $k$ th layer and the node  $y$  of the  $l$ th layer are not connected, whereas  $b_{xy}^{k,l} = 1$  implies that they are connected. Since the network is undirected,  $\mathcal{A}$  has an overall real-symmetric structure. The overall dimension of  $\mathcal{A}$  is  $n \times n$  where  $n = n_1 + n_2 + \dots + n_m$ .

It should be noted that the diagonal blocks are necessarily square, whereas the off-diagonal blocks may be rectangular in general. In case there are no interlayer connections, then all off-diagonal blocks are zero matrices, and  $\mathcal{A}$  is a block-diagonal matrix. The other extreme is that when there is no intra-layer connection, then the diagonal blocks would be zero matrices. For multiplex networks, inter-layer edges can only connect nodes representing the same entity in different layers. Therefore,  $n_1 = n_2 = \dots = n_m$  and the off-diagonal blocks would be identity matrices in this case.

Finally, instead of binary values of 0 and 1 for the elements, we may consider any real number from the interval  $[0, 1]$ , in which case we have an adjacency matrix

corresponding to a weighted network.

### B. Spectral Fluctuation Properties in RMT

Spectral fluctuations of the eigenvalues of an operator associated with the system can reveal essential information about its underlying dynamics. The agreement of these fluctuations with the predicted results of RMT serves as an indicator of chaotic or complex behavior of the system. Among the various measures for quantifying short-range spectral fluctuations, the distribution of spacing ratios stands out as a widely used measure. Its appeal lies in the fact that it does not require prior knowledge of the local density of states, thereby circumventing the need for spectral unfolding [36, 37].

Let us consider the ordered set of eigenvalues  $\{\lambda_1, \lambda_2, \dots, \lambda_n\}$  obtained from diagonalizing a given matrix. The consecutive spacing ratios are then defined as

$$r_j = \frac{\lambda_{j+2} - \lambda_{j+1}}{\lambda_{j+1} - \lambda_j}, \quad j = 1, 2, \dots, n-2. \quad (2)$$

The distribution of these spacing ratios, called the spacing ratio distribution (SRD), is known [36, 37] for the classical Gaussian random matrix ensembles and is given by

$$P(\alpha, r) = C_\alpha \frac{(r + r^2)^\alpha}{(1 + r + r^2)^{1+3\alpha/2}}, \quad (3)$$

where  $C_\alpha$  is the normalization factor such that  $\int_0^\infty P(\alpha, r) dr = 1$ . The parameter  $\alpha$  in the above expression is related to the symmetry properties of the random matrix under consideration and coincides with the Dyson index ( $\beta$ ) for the classical random matrix ensembles [38]. Therefore, it assumes the values 1, 2, and 4 for the Gaussian orthogonal ensemble (GOE), Gaussian unitary ensemble (GUE), and Gaussian symplectic ensemble (GSE), respectively, characterizing real-symmetric, complex-Hermitian, and quaternion self-dual random matrices having zero-mean Gaussian entries, respectively. Remarkably, by appropriately fixing the parameter  $\alpha$ , the above formula has also been found to work for higher-order spacing ratios, as well as in the case of matrices having a block-diagonal structure.

In the past few years, higher-order spacing ratios, beyond the nearest-neighbor ratio defined in Eq. (2), have been investigated and applied in various contexts such as quantum chaos, many-body non-integrability, and Floquet dynamics [39–41]. A notable example is that of  $k$ -th order (non-overlapping) spacing ratio, defined as [39, 42, 43]

$$r_i^{(k)} = \frac{\lambda_{i+2k} - \lambda_{i+k}}{\lambda_{i+k} - \lambda_i}, \quad i, k = 1, 2, 3, \dots \quad (4)$$

For  $k = 1$ , one recovers Eq. (2). In Ref. [39],  $k$ th order spacing ratio has been used to study the superposition of

$k \backslash m$	1	2	3	4
1	1	$\sim 0$	$\sim 0$	$\sim 0$
2	4	2	$\sim 1.25$	1
3	8	4	3	$\sim 2.5$
4	13	7	5	4

TABLE I. Tabulation of higher-order indices  $\alpha$  for various  $k$  and superposition of  $m$  GOEs.

random matrix spectra. Evidently, one can also examine block diagonal random matrices, where each block corresponds to one of the standard classical ensembles, e.g., we can have a direct sum of two GOE matrices. For these cases, it is possible to find some appropriate value of  $\alpha$  [39], such that the  $k$ -th order spacing ratio distribution for the full set of eigenvalues aligns with Eq. (3). In the present work, we will be working with real-symmetric matrices, for which we list the  $\alpha$  values to be used for a given  $k$  value for the order of the spacing ratio and the number  $m$  of diagonal blocks, in Table I.

It should be noted that the GOE matrices constituting the diagonal blocks should be identically distributed to give rise to the fluctuation properties consistent with Eq. (3) with an appropriate value of  $\alpha$  as listed in Table I. In other words,  $\langle \text{tr}(A^{(j)})^2 \rangle / (n_j + 1)$ , which reflects a normalized variance, should be the same for all the diagonal blocks  $A_{n_j \times n_j}^{(j)}$ , where  $\langle \cdot \rangle$  denotes ensemble averaging [38]. If this is not the case, then the blocks need to be scaled to lead to spectral fluctuations consistent with the RMT results. For instance, suppose in a two-diagonal block case, the respective matrices are taken from distributions  $P(A^{(j)}) \propto \exp \left[ -\frac{1}{2\sigma_j^2} \text{tr}(A^{(j)})^2 \right]; j = 1, 2$ , then  $\langle \text{tr}(A^{(j)})^2 \rangle / (n_j + 1) = n_j \sigma_j^2 / 2$ . In this case, the rescaled diagonal blocks to be used are  $\tilde{A}^{(j)} = a A^{(j)} / (n_j \sigma_j^2 / 2)^{1/2}$ , where  $a$  could be an arbitrary nonzero constant [44, 45]. Similar considerations must be taken when random adjacency matrices are constructed using Erdős-Rényi (ER) random graphs, as will be seen in the next section.

### III. SPECTRAL FLUCTUATIONS OF RANDOM MULTILAYER NETWORK

Random networks are prevalent in diverse real-world systems, including social structures, biological interactions, and technological infrastructures such as the internet [46–51]. In social contexts, connections—like friendships—often form without a fixed pattern, while in biological systems, interactions among proteins or neurons can exhibit similar randomness. Even the internet, with its vast web of interconnected websites and pages, exhibits characteristics of a random network. Despite their differences, these systems often display universal spectral properties well captured by RMT [22, 23]. In this section, we investigate spectral fluctuations in multilayer random networks, focusing on how variations in connec-

tion patterns across and within layers impact spectral fluctuations.

For our analyses, we construct blocks of the overall adjacency matrix using the Erdős-Rényi (ER) approach. The  $j$ th diagonal block  $A_{n_j \times n_j}^j$  is constructed using the usual Erdős-Rényi  $G(n_j, p_j)$  graph model in which the  $n_j$  nodes (vertices) are connected randomly in a manner such that each edge is included in the graph with probability  $p_j$ , independently from every other edge. Consequently, a graph in  $G(n_j, p_j)$  has on an average  $n_j(n_j - 1)p_j/2$  edges. To keep the variances comparable, we multiply the  $j$ th block by a factor of  $1/\sqrt{4n_j p_j(1 - p_j)}$ . This ensures that the trace of the second moment  $\langle \text{tr}(A_j^2) \rangle$  remains comparable across blocks. In this way, the diagonal blocks retain similar spectral fluctuations, ensuring agreement with the results of random matrix theory (RMT). If the blocks are not scaled to have comparable variances, the resulting spectral fluctuations deviate from the RMT predictions because of the statistical mismatch across layers.

An off-diagonal block  $B_{n_j \times n_k}^{j,k}$  is also constructed in a similar manner by connecting the  $n_j$  nodes of the  $j$ th layer with the  $n_k$  nodes of the  $k$ th with probability  $p_{jk}$ ,  $j \neq k$ . Thus, on average, there will be  $n_j n_k p_{jk}$  edges between the two layers. To match the variances across all blocks, we scale the off-diagonal blocks by the factor  $1/\sqrt{4\sqrt{n_j n_k} p_{jk}(1 - p_{jk})}$ .

Additionally, we will consider the case of multiplex networks for which inter-layer edges connect the same nodes across all the layers, and therefore all off-diagonal blocks of  $\mathcal{A}$  are identity matrices.

We consider the following four different types of possibilities, as also depicted in Fig. 1.

*Case a:* In this case, there are no connections between nodes of different layers ( $p_{jk} = 0$  for all  $j \neq k$ ) and therefore all off-diagonal blocks in the adjacency matrix  $\mathcal{A}$  are zero matrices. The diagonal blocks associated with the intra-layer connections have random entries 0 or 1 as decided by the Erdős-Rényi construction. The  $\mathcal{A}$  matrix in this case, therefore, assumes a block-diagonal form.

*Case b:* In this case, we consider both intra-layer and inter-layer nodes randomly connected, the adjacency matrix of the multilayer network is overall random.

*Case c:* This is the case corresponding to a multiplex network, so the off-diagonal blocks are identity matrices. Randomness comes from diagonal blocks.

*Case d:* Here, we consider no intra-layer connections ( $p_j = 0$  for all  $j$ ). Consequently, all diagonal blocks in  $\mathcal{A}$  are zero matrices, and the off-diagonal blocks for inter-layer connections contain random 0 or 1 entries.

In this study, for simplicity, we focus on bilayer ( $m = 2$ ) and trilayer ( $m = 3$ ) networks to examine their spectral fluctuations, particularly for higher-order fluctuations where  $k \geq 2$ . For  $k = 1$ , only single-layer networks ( $m = 1$ ) exhibit a correlated spacing ratio distribution (SRD), while bilayer and trilayer networks display an uncorrelated spacing ratio distribution, as illustrated in Fig. 2, which also conforms to Table I. Thus, to ensure consistency, we only use higher-order spectral fluctuation measurements across all network configurations.

Before turning to the multilayer network cases, it is instructive to examine the consequences of not scaling the diagonal and the off-diagonal blocks discussed earlier. We consider a bilayer network ( $m = 2$ ) under *case a*, where the two layers have significantly different connection probabilities. Without scaling, the eigenvalue distributions yield spacing ratio statistics that deviate from RMT expectations and do not correspond to any well-defined  $\alpha$  value. This is evident in Fig. 3, where the second-order ( $k = 2$ ) and third-order ( $k = 3$ ) spacing ratio distributions fail to align with Eq. (3) for any  $\alpha$ . Upon applying the appropriate scaling, as we will see in the next subsection, the distributions exhibit excellent agreement with RMT predictions for  $\alpha = 2$  and  $\alpha = 4$ , respectively. Hereafter, we always implement the appropriate scaling for each block (diagonal and off-diagonal) to examine the fluctuation properties.

### A. Multilayer network without inter-layer connections

This corresponds to *case a*, all the off-diagonal blocks of the adjacency matrix  $\mathcal{A}$  are zero matrices. We examine spectral fluctuations considering various choices of edge connection probability  $p_j$  for diagonal blocks, which will help us corroborate the universality aspect of spectral fluctuations. In RMT terminology, this case would correspond to the direct sum of  $m$  GOE's for a  $m$  layer network [39]. By multiplying the  $j$ th block by a scaling factor, we ensure that the SRD aligns more closely with the RMT predictions, as illustrated in Figs. 4 and 5.

In Fig. 4, we observe that for a bi-layer block structure, the distributions correspond to  $\alpha = 2$  and  $\alpha = 4$  for  $k = 2$  and  $k = 3$ , respectively, across different combinations of edge connection probability  $p_j$  in the layers. Similarly, Fig. 5 illustrates that for a trilayer block structure, the distributions correspond to  $\alpha = 3$  and  $\alpha = 5$  for  $k = 3$  and  $k = 4$ , respectively, under various combinations of edge connection probability  $p_j$  in the layers.

### B. Multilayer network with both inter-layer and intra-layer connections

In this setup, all blocks of the adjacency matrix  $\mathcal{A}$  are connected with edges defined by specific connection probabilities; this aligns with *case b*. Spectral fluctuations are analyzed by exploring various edge connection probabilities  $p_j$  for diagonal blocks and  $p_{jk}$  for off-diagonal blocks. In the context of RMT, this scenario corresponds directly to a single GOE representing an  $m$ -layer network.

We analyze SRD for a bilayer network with  $k = 2$  and



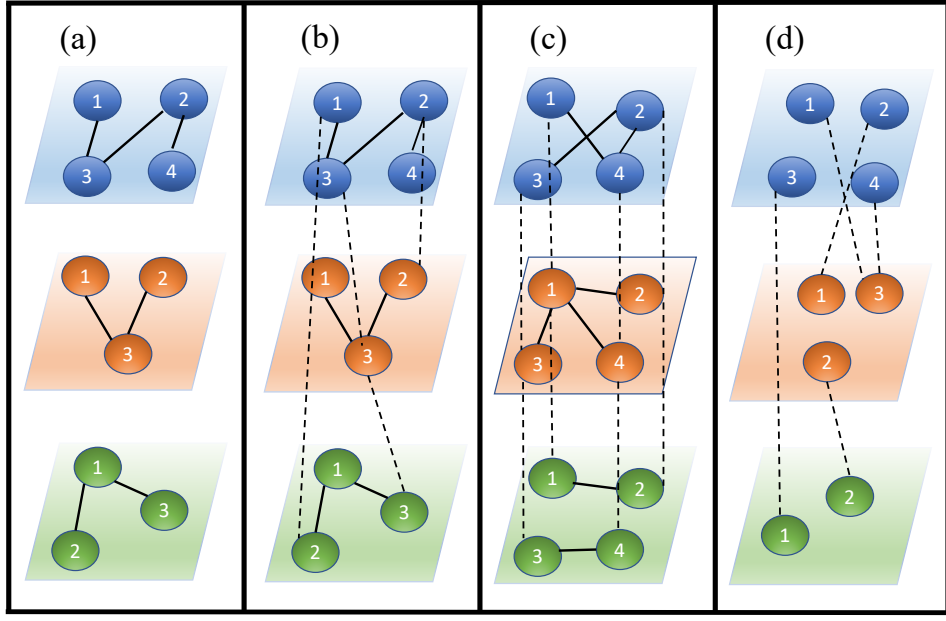


FIG. 1. Schematic diagram representing examples of multilayer networks. The black dashed line indicates an inter-layer connection, while the solid black line depicts an intra-layer connection. (a) A multilayer network with only intra-layer connections, no inter-layer connections. (b) A general multilayer network where inter-layer edges connect different nodes across the layers. (c) A multiplex network where the inter-layer edges connect the same nodes across the layers. (d) Multiparite network with only inter-layer connections, no intra-layer connections.

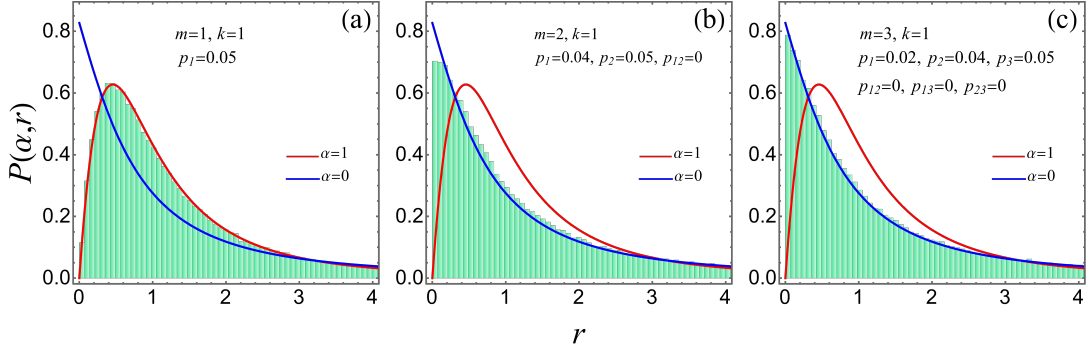


FIG. 2. The first-order ( $k = 1$ ) SRD plots (histogram) is obtained through simulations based on an ensemble of 250 adjacency matrices  $\mathcal{A}$  for three network configurations: (a) a single-layer network with dimensions  $n_1 = 800 \times 800$  and an edge connection probability of  $p_1 = 0.05$ ; (b) a bilayer network comprising block-diagonal matrices of dimensions  $n_1 = 350 \times 350$  and  $n_2 = 450 \times 450$ , with edge connection probabilities  $p_1 = 0.04$ ,  $p_2 = 0.05$ , and no inter-layer connections ( $p_{12} = 0$ ); and (c) a trilayer network with block-diagonal matrices of dimensions  $200 \times 200$ ,  $300 \times 300$ , and  $500 \times 500$ , with edge connection probabilities  $p_1 = 0.02$ ,  $p_2 = 0.04$ ,  $p_3 = 0.05$ , and no inter-layer connections ( $p_{12} = 0$ ,  $p_{13} = 0$ ,  $p_{23} = 0$ ).

$k = 3$ , finding that they correspond to  $\alpha = 4$  and  $\alpha = 8$ , respectively, as shown in Fig. 6. As indicated in Table I, these  $\alpha$  and  $k$  values are representative of a single-layer network ( $m = 1$ ). Similarly, for a trilayer network with  $k = 3$  and  $k = 4$ , the results correspond to  $\alpha = 8$  and  $\alpha = 13$ , respectively, as illustrated in Fig. 7, aligning once more with the behavior expected for a single-layer network, as per Table I.

Next, we investigate the adjacency matrix  $\mathcal{A}$  for a multiplex network, *case c*, where the off-diagonal blocks are identity matrices, and randomness comes due to differ-

ent edge connection probability ( $p_j$ ) of intra-layer connections. In this case too, we find that the SRD for the bilayer network with  $k = 2$  and  $k = 3$  corresponds to  $\alpha = 4$  and  $\alpha = 8$ , respectively. Similarly, for the trilayer network with  $k = 3$  and  $k = 4$ , the SRD values correspond to  $\alpha = 8$  and  $\alpha = 13$ , respectively. These findings also indicate that the SRD aligns with that of a single-layer network, as indicated in Table I.

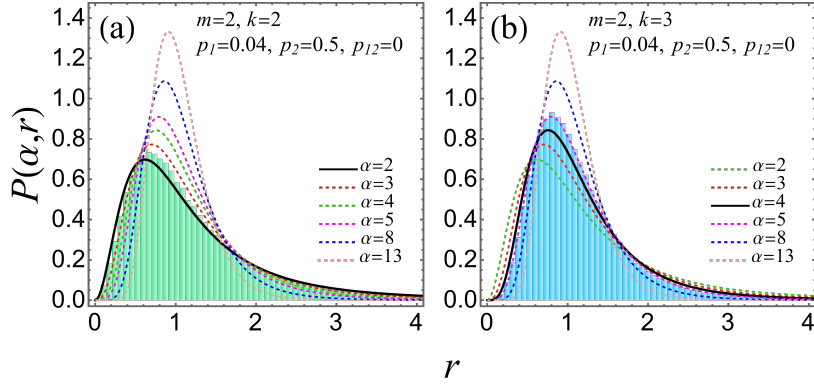


FIG. 3. Higher order SRD plots (histogram) for bilayer network ( $m = 2$ ) with no inter-layer connections (case a) without scaling of the two blocks. The connection probabilities being very different in the two layers lead to outcomes different from RMT predictions. The diagonal blocks of the adjacency matrix  $\mathcal{A}$  are of dimension  $350 \times 350$  and  $450 \times 450$ , respectively. The histograms have been obtained using simulations based on an ensemble comprising 250 adjacency matrices. The order of the spacing distribution and edge probabilities,  $(k, p_1, p_2)$  for the histograms obtained from numerical simulations are (a)  $(2, 0.04, 0.5)$ , (b)  $(3, 0.04, 0.5)$ .

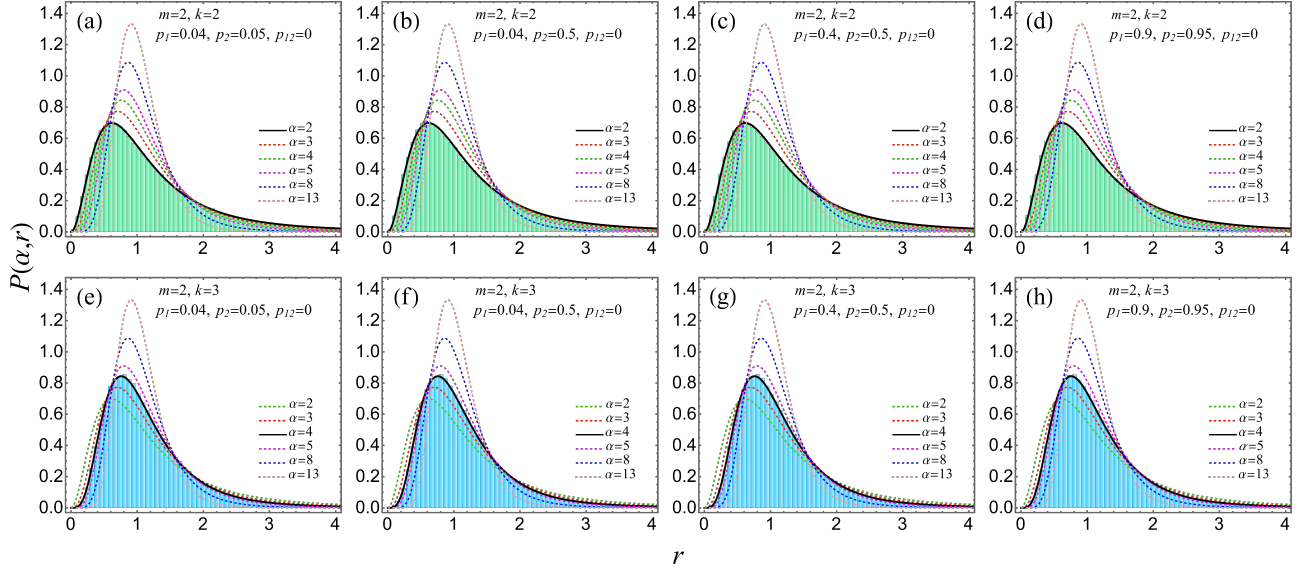


FIG. 4. Higher order SRD plots (histogram) for bilayer network ( $m = 2$ ) with no inter-layer connections (case a). The diagonal blocks of the adjacency matrix  $\mathcal{A}$  are of dimension  $350 \times 350$  and  $450 \times 450$ , respectively. The histograms have been obtained using simulations based on an ensemble comprising 250 adjacency matrices. The order of the spacing distribution and edge probabilities,  $(k, p_1, p_2)$  for the histograms obtained from numerical simulations are (a)  $(2, 0.04, 0.05)$ , (b)  $(2, 0.04, 0.5)$ , (c)  $(2, 0.4, 0.5)$ , (d)  $(2, 0.9, 0.95)$ , (e)  $(3, 0.04, 0.05)$ , (f)  $(3, 0.04, 0.5)$ , (g)  $(3, 0.4, 0.5)$ , and (h)  $(3, 0.9, 0.95)$ .

### C. Multilayer network with no intra-layer connections

This is *case d*, all diagonal blocks of the adjacency matrix  $\mathcal{A}$  are zero matrices. We examine spectral fluctuations by considering various choices of the edge connection probability  $p_{jk}$  for the off-diagonal blocks. In RMT terminology, this case would also correspond directly to a single GOE representing an  $m$ -layer network.

We examined the SRD for the bilayer network with  $k = 2$  and  $k = 3$ , finding that they correspond to  $\alpha =$

4 and  $\alpha = 8$ , respectively, as shown in Fig. 8, which aligns with the single-layer network case, as indicated in Table I. Similarly, for the trilayer network with  $k = 3$  and  $k = 4$ , the SRD values match with  $\alpha = 8$  and  $\alpha = 13$ , respectively, as illustrated in Fig. 9, and they also correspond to the single-layer network case, as suggested by Table I.

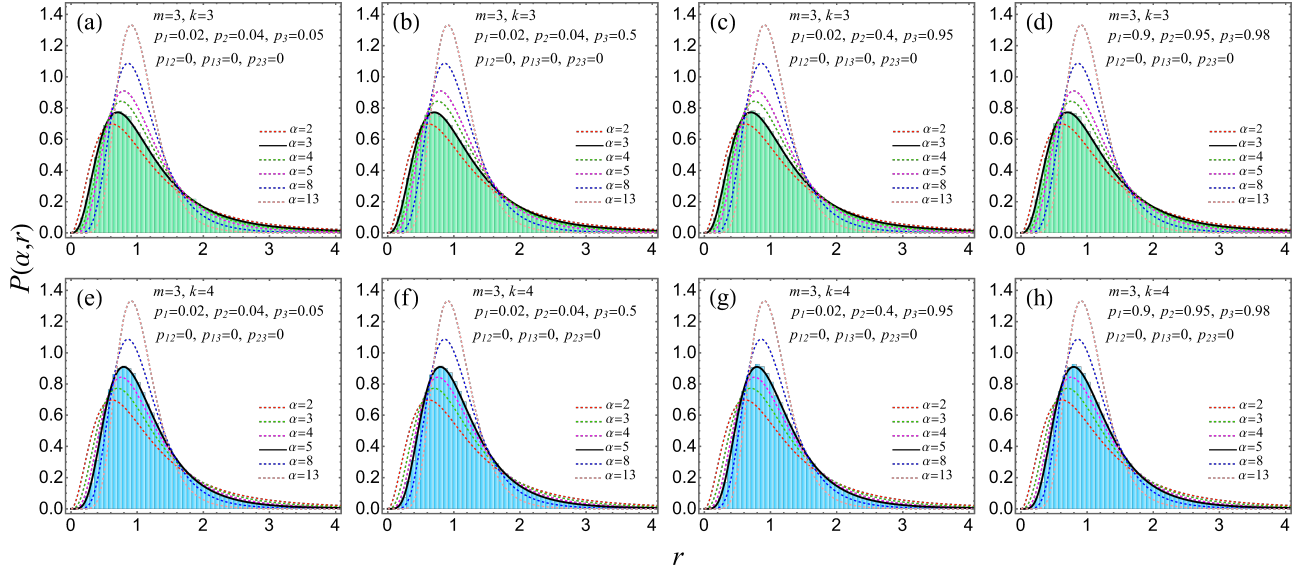


FIG. 5. Higher order SRD plots (histogram) for trilayer network ( $m = 3$ ) with no inter-layer connections (case a). The diagonal blocks of the adjacency matrix  $\mathcal{A}$  are of dimension  $200 \times 200$ ,  $300 \times 300$  and  $500 \times 500$ , respectively. The histograms have been obtained using simulations based on an ensemble comprising 200 adjacency matrices. The order of the spacing distribution and edge probabilities,  $(k, p_1, p_2, p_3)$  for the histograms obtained from numerical simulations are (a)  $(3, 0.02, 0.04, 0.05)$ , (b)  $(3, 0.02, 0.04, 0.5)$ , (c)  $(3, 0.02, 0.4, 0.95)$ , (d)  $(3, 0.9, 0.95, 0.98)$ , (e)  $(4, 0.02, 0.04, 0.05)$ , (f)  $(4, 0.02, 0.04, 0.5)$ , (g)  $(4, 0.02, 0.4, 0.95)$ , and (h)  $(4, 0.9, 0.95, 0.98)$ .

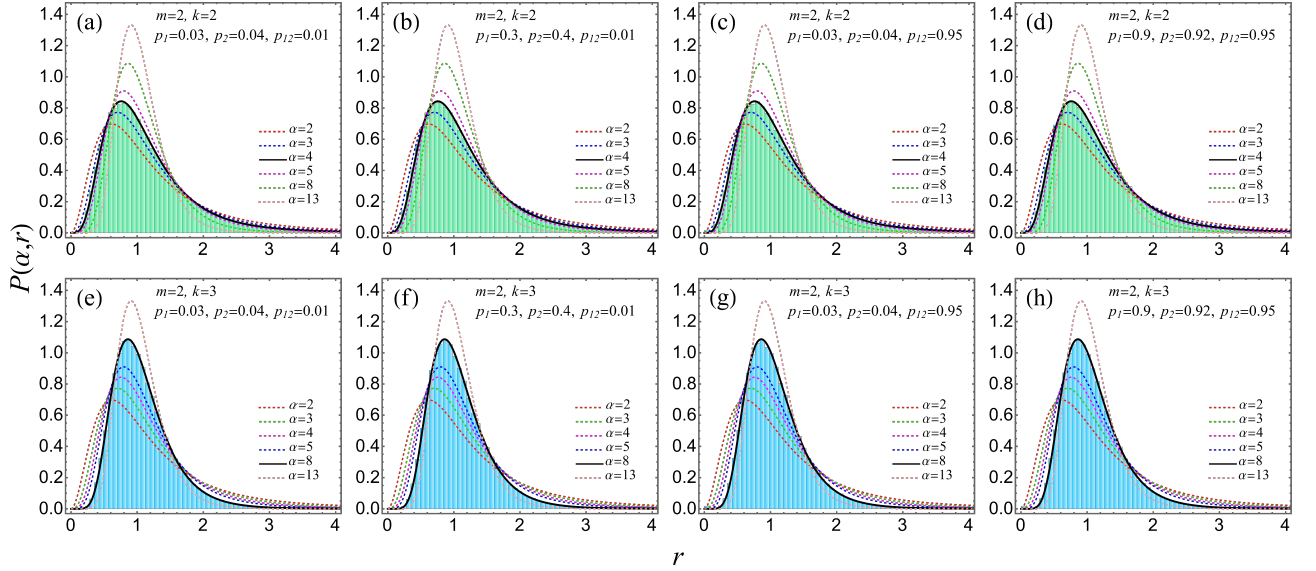


FIG. 6. Higher order SRD plots (histogram) for bilayer network ( $m = 2$ ) with intra-layer and inter-layer connections (case b). The diagonal blocks of the adjacency matrix  $\mathcal{A}$  are of dimension  $350 \times 350$  and  $450 \times 450$ , respectively. The histograms have been obtained using simulations based on an ensemble comprising 250 adjacency matrices. The order of the spacing distribution and edge probabilities,  $(k, p_1, p_2, p_{12})$  for the histograms obtained from numerical simulations are (a)  $(2, 0.03, 0.04, 0.01)$ , (b)  $(2, 0.3, 0.4, 0.01)$ , (c)  $(2, 0.03, 0.04, 0.95)$ , (d)  $(2, 0.9, 0.92, 0.95)$ , (e)  $(3, 0.03, 0.04, 0.01)$ , (f)  $(3, 0.3, 0.4, 0.01)$ , (g)  $(3, 0.03, 0.04, 0.95)$ , and (h)  $(3, 0.9, 0.92, 0.95)$ .

#### D. A crossover model for the bilayer network

In the previous three subsections III A-III C, we demonstrated that the higher-order SRD of the (scaled)

eigenvalues of the adjacency matrix for different types of multilayer networks is in remarkable agreement with the predictions from RMT. To further investigate the fluctuation properties through SRD in a bilayer network, we

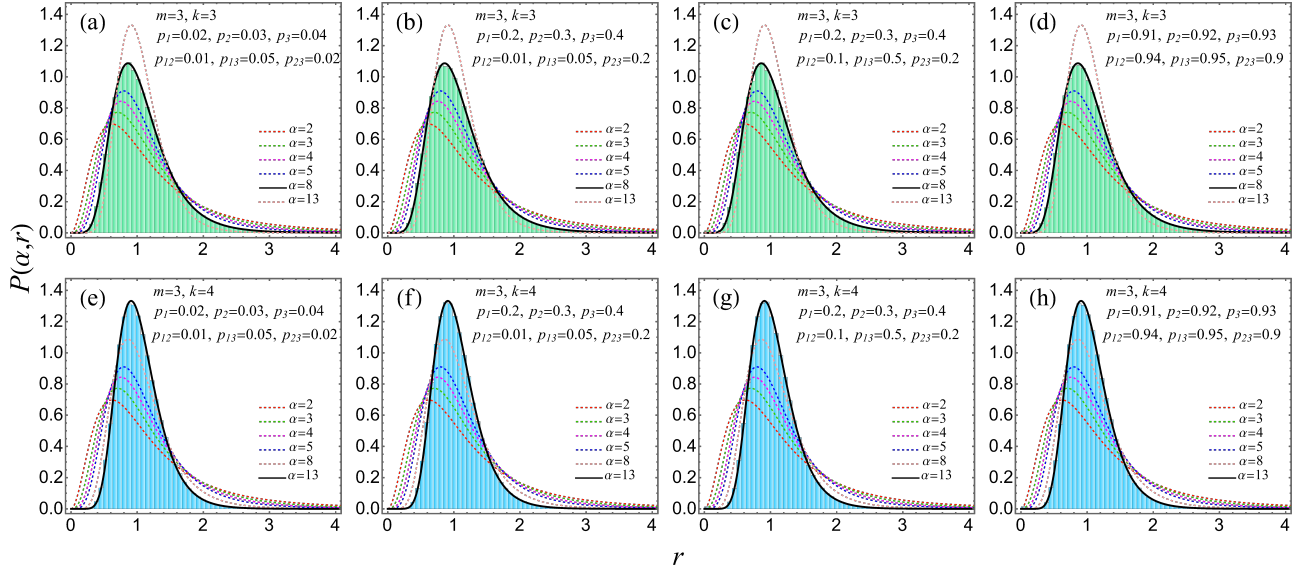


FIG. 7. Higher order SRD plots (histogram) for trilayer network ( $m = 3$ ) with intra-layer and inter-layer connections (case b). The diagonal blocks of the adjacency matrix  $\mathcal{A}$  are of dimension  $200 \times 200$ ,  $300 \times 300$  and  $500 \times 500$ , respectively. The histograms have been obtained using simulations based on an ensemble comprising 200 adjacency matrices. The order of the spacing distribution and edge probabilities,  $(k, p_1, p_2, p_3, p_{12}, p_{13}, p_{23})$  for the histograms obtained from numerical simulations are (a)  $(3, 0.02, 0.03, 0.04, 0.01, 0.05, 0.02)$ , (b)  $(3, 0.2, 0.3, 0.4, 0.01, 0.05, 0.2)$ , (c)  $(3, 0.2, 0.3, 0.4, 0.9, 0.5, 0.2)$ , (d)  $(3, 0.91, 0.92, 0.93, 0.95, 0.95, 0.9)$ , (e)  $(4, 0.02, 0.03, 0.04, 0.01, 0.05, 0.02)$ , (f)  $(4, 0.2, 0.3, 0.4, 0.01, 0.05, 0.2)$ , (g)  $(4, 0.2, 0.3, 0.4, 0.9, 0.5, 0.2)$ , and (h)  $(4, 0.91, 0.92, 0.93, 0.95, 0.95, 0.9)$

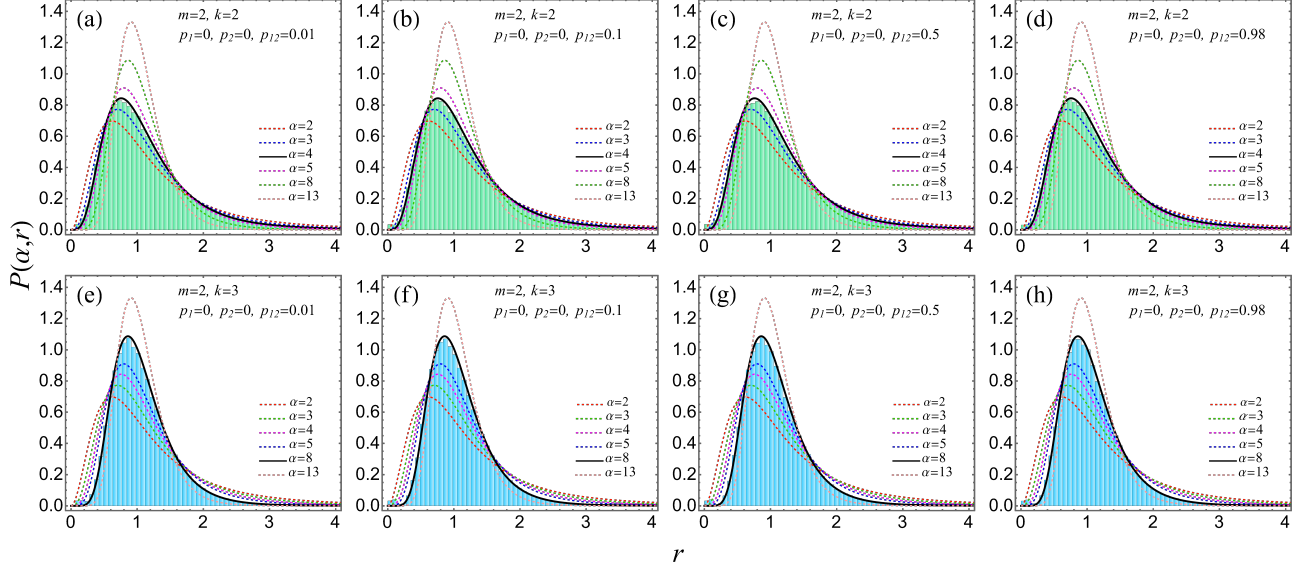


FIG. 8. Higher order SRD plots (histogram) for bilayer network ( $m = 2$ ) with no intra-layer connections (case d). The diagonal blocks of the adjacency matrix  $\mathcal{A}$  are of dimension  $350 \times 350$  and  $450 \times 450$ , respectively. The histograms have been obtained using simulations based on an ensemble comprising 250 adjacency matrices. The order of the spacing distribution and edge probabilities,  $(k, p_{12})$  for the histograms obtained from numerical simulations are (a)  $(2, 0.01)$ , (b)  $(2, 0.1)$ , (c)  $(2, 0.5)$ , (d)  $(2, 0.98)$ , (e)  $(3, 0.01)$ , (f)  $(3, 0.1)$ , (g)  $(3, 0.5)$ , and (h)  $(3, 0.98)$

introduce a crossover model, defined as follows

$$(1 - \gamma) \begin{bmatrix} A_{n_1 \times n_1}^1 & 0 \\ 0 & A_{n_2 \times n_2}^2 \end{bmatrix} + \gamma \begin{bmatrix} 0 & B_{n_1 \times n_2}^{1,2} \\ (B_{n_2 \times n_1}^{1,2})^T & 0 \end{bmatrix}. \quad (5)$$

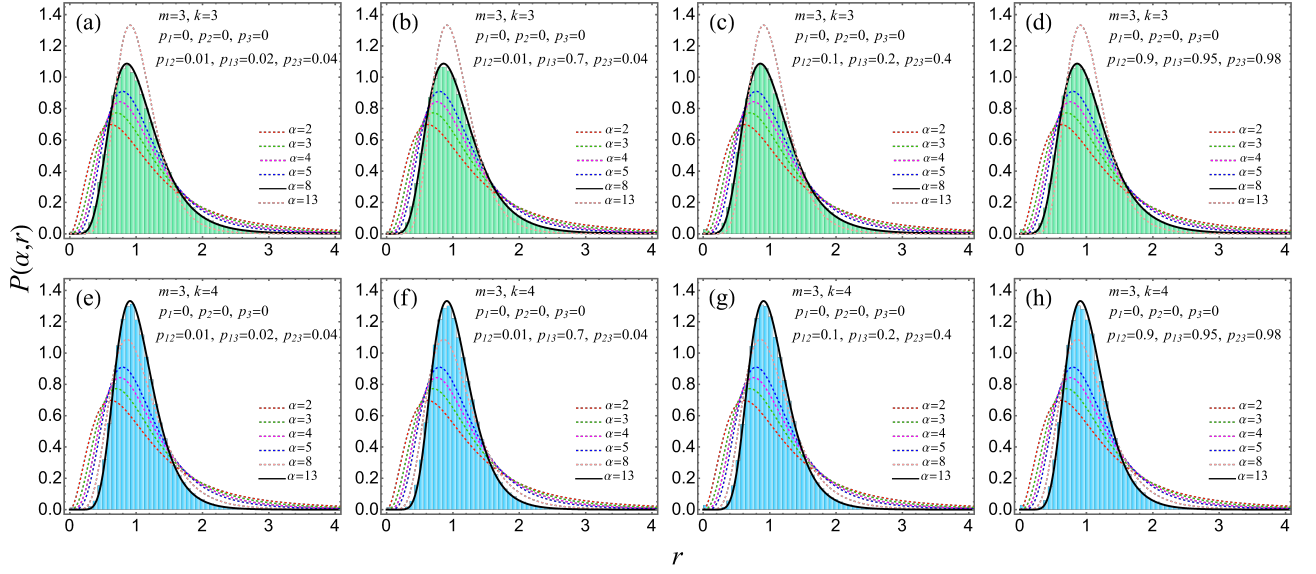


FIG. 9. Higher order SRD plots (histogram) for trilayer network ( $m = 3$ ) with no intra-layer connections (case d). The diagonal blocks of the adjacency matrix  $\mathcal{A}$  are of dimension  $200 \times 200$ ,  $300 \times 300$  and  $500 \times 500$ , respectively. The histograms have been obtained using simulations based on an ensemble comprising 200 adjacency matrices. The order of the spacing distribution and edge probabilities,  $(k, p_{12}, p_{13}, p_{23})$  for the histograms obtained from numerical simulations are (a)  $(3, 0.01, 0.02, 0.04)$ , (b)  $(3, 0.01, 0.7, 0.04)$ , (c)  $(3, 0.1, 0.2, 0.4)$ , (d)  $(3, 0.9, 0.95, 0.98)$ , (e)  $(4, 0.01, 0.02, 0.04)$ , (f)  $(4, 0.01, 0.7, 0.04)$ , (g)  $(4, 0.1, 0.2, 0.4)$ , and (h)  $(4, 0.9, 0.95, 0.98)$

Here,  $\gamma$  is a crossover parameter,  $A_{n_1 \times n_1}^1$  and  $A_{n_2 \times n_2}^2$  are the block matrices corresponding to intra-layer connections of layers 1 and 2, respectively. The matrix  $B_{n_1 \times n_2}^{1,2}$  represents inter-layer connections between the two layers, and  $(B_{n_1 \times n_2}^{1,2})^T$  is the transpose of  $B_{n_1 \times n_2}^{1,2}$ . The blocks  $A_{n_1 \times n_1}^1$ ,  $A_{n_2 \times n_2}^2$ , and  $B_{n_1 \times n_2}^{1,2}$  are constructed from the ER network, with edge connection probabilities  $p_1$ ,  $p_2$ , and  $p_{12}$ , respectively. The parameter  $\gamma$  can vary from 0 to 1, with the extremes corresponding to only intra-layer connections ( $\gamma = 0$ ) and only inter-layer connections ( $\gamma = 1$ ). When  $\gamma = 0$ , the model reduces to a block diagonal structure, leading to two GOEs for the  $m = 2$  layer network, as seen in III A. When  $\gamma = 1$ , the model converges to a single GOE, as observed in III C. In this section, we focus on how the SRD statistics evolve with varying values of intermediate  $\gamma$ . Specifically, we examine up to which value of  $\gamma$  the SRD exhibits statistics corresponding to  $m = 2$  (two GOEs), and after which value of  $\gamma$  it transitions to  $m = 1$  (a single GOE). Essentially,  $\gamma$  serves as a strength factor for the off-diagonal blocks (or inter-layer connectivity); as  $\gamma$  increases, the strength of the off-diagonal blocks increases while the strength of the diagonal blocks decreases and vice versa, for fixed values of  $p_1$ ,  $p_2$ , and  $p_{12}$ .

In Fig. 10, we investigate the second-order ( $k = 2$ ) SRD for our crossover model. The (scaled) blocks are  $A_{350 \times 350}^1$ ,  $A_{450 \times 450}^2$ , and  $B_{350 \times 450}^{1,2}$ , and we vary the crossover parameter  $\gamma$ . When  $\gamma = 0.01$ , the system effectively exhibits a two block-diagonal structure ( $m = 2$ ), representing two weakly connected GOE layers, in line

with Table I, as the histogram aligns closely with the  $\alpha = 2$  result from RMT. As we gradually increase the value of  $\gamma$ , we observe intermediate statistics that show the transition from two GOEs to a single GOE. At  $\gamma = 0.06$ , the SRD histogram aligns closely with the  $\alpha = 4$  result from RMT, corresponding to a single GOE ( $m = 1$ ), as indicated by Table I. Furthermore, we find that the crossover behavior remains independent of the intra-layer and inter-layer edge connection probabilities, provided the network dimensions are fixed. For example, as shown in Fig. 10 (a), (e), and (i), the statistics remain consistent for  $\gamma = 0.01$  despite the different edge connection probabilities. Additionally, we examined the third-order ( $k = 3$ ) SRD for the same dimensions and observed a similar transition in SRD statistics, from two GOEs to a single GOE, as  $\gamma$  is varied.

We also observed that similar statistics are seen for larger dimensions of our model. In addition, we have also found that even for small  $\gamma > 0$ , the spectral fluctuations correspond to a single GOE. The larger the model's dimensions (bilayer network), the faster the crossover and vice versa. These results highlight how essential it is to employ appropriate scaling factors when investigating multilayer network architectures to obtain consistency with RMT predictions.



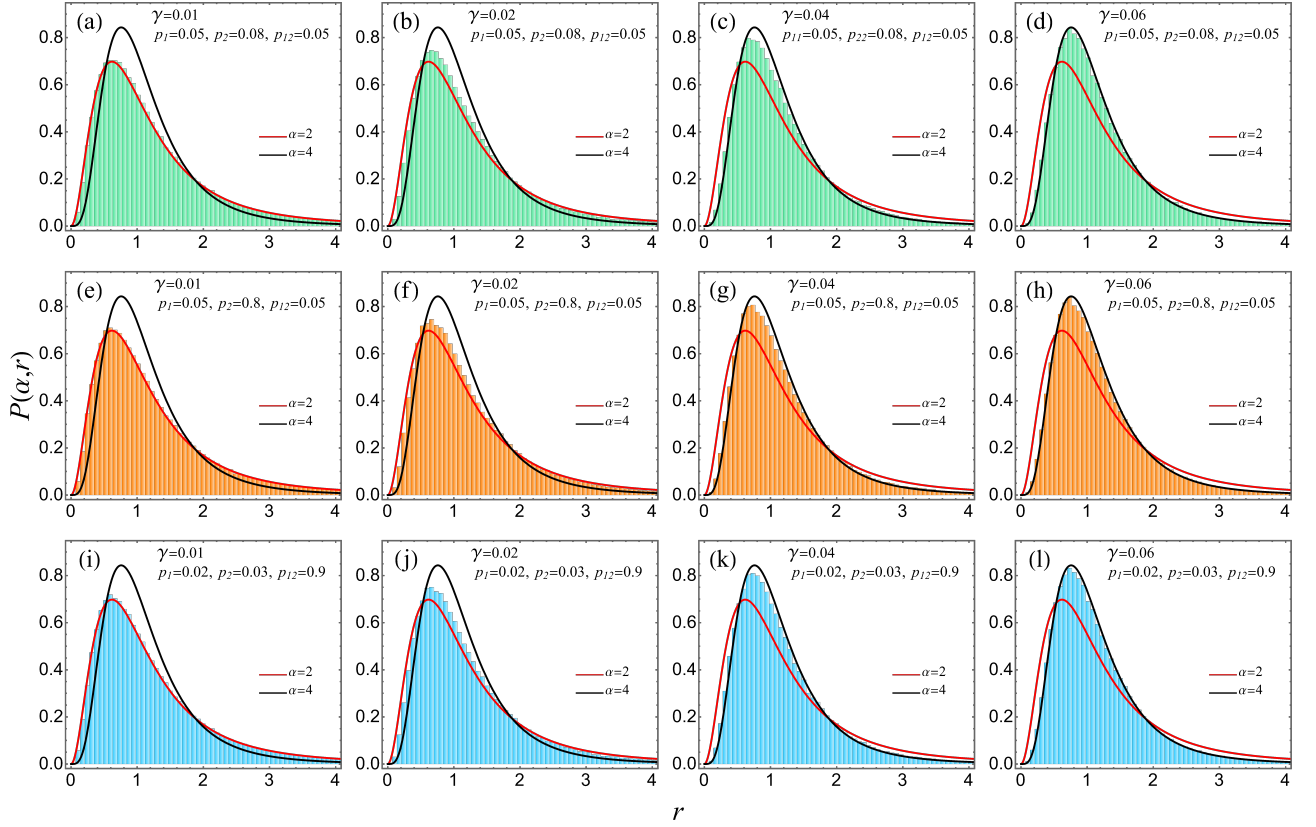


FIG. 10. Second order ( $k = 2$ ) SRD plots (histogram) for bilayer network ( $m = 2$ ) for our crossover model which is mentioned in subsection IIID. The diagonal blocks of the adjacency matrix of model are of dimension  $350 \times 350$  and  $450 \times 450$ , respectively. The histograms have been obtained using simulations based on an ensemble comprising 250 adjacency matrices. The crossover parameter and edge probabilities,  $(\gamma, p_1, p_2, p_{12})$  for the histograms obtained from numerical simulations are (a) (0.01, 0.05, 0.08, 0.05), (b) (0.02, 0.05, 0.08, 0.05), (c) (0.04, 0.05, 0.08, 0.05), (d) (0.06, 0.05, 0.08, 0.05), (e) (0.01, 0.05, 0.8, 0.05), (f) (0.02, 0.05, 0.8, 0.05), (g) (0.04, 0.05, 0.8, 0.05), (h) (0.06, 0.05, 0.8, 0.05), (i) (0.01, 0.02, 0.03, 0.9), (j) (0.02, 0.02, 0.03, 0.9), (k) (0.04, 0.02, 0.03, 0.9), and (l) (0.06, 0.02, 0.03, 0.9)

#### IV. APPLICATION OF SPECTRAL FLUCTUATIONS OF RANDOM MULTILAYER NETWORK

In this section, we explore the application of a multilayer network approach to analyze the complexity of protein structures [51, 52]. When modeling proteins as networks, a node can represent an atom, residue, or structural element, while the edges (connections) between these nodes signify various types of interactions, such as covalent bonds, hydrogen bonds, or spatial proximity [53].

In our study, we employed the distance matrix as an adjacency matrix, interpreting the spatial distances between atoms or residues as a measure of connectivity or interaction strength. This approach proves valuable in structural and functional analyses of proteins as it highlights how the three-dimensional arrangement of a protein influences its interactions and also reveals the universal features captured by RMT. To construct the adjacency matrix from the distance matrix, a threshold is typically applied to determine whether two node atoms (or

residues) are considered adjacent. Specifically, if the distance between two atoms falls below a predefined threshold, they are regarded as adjacent, and the corresponding adjacency matrix entry  $a_{xy}$  is assigned a value of 1; otherwise, they are considered not connected and  $a_{xy}$  is set to 0.

We study the spectral fluctuation of interatomic distance networks in protein crystals for two different species within the framework of random matrix theory.

(a) We consider two proteins (1EWT and 1EWK) of *Rattus norvegicus*. 1EWT and 1EWK exhibit the global stoichiometry characteristic of a homodimer (homo 2-mer). While both are X-ray crystal structures of the metabotropic glutamate receptor subtype 1, 1EWT represents the free form (not bound to any ligand or small molecule), and 1EWK is the protein complexed with glutamate (a small molecule). Both proteins have a deposited residue count of 980. However, the number of modeled residues differs: 912 residues are modeled for 1EWT, while 897 residues are modeled for 1EWK.

(b) The 1UW6 protein from *Lymnaea stagnalis* exhibits cyclic global symmetry and global stoichiometry

consistent with a pentameric assembly (Homo 5-mer) and X-ray structure of acetylcholine binding receptor. It has a deposited residue count of 4,220, while the number of modeled residues is 4,134.

To analyze the fluctuation properties in protein structures, we employed the spacing ratio distribution (SRD) alongside the cumulative SRD (CSRSD). The explicit formulae for the CSRSD are provided in Appendix A for different  $\alpha$  values, which are used in our analysis. In Section II, we have discussed the scaling factors for the diagonal and off-diagonal terms of the adjacency matrix of a multilayer network in terms of the dimension of the network and the probabilities of edge connection. However, in real networks, the number of edges is typically known. Therefore, we can explicitly redefine the scaling factors in terms of the number of edges and the dimensions of the blocks. The scaling factor for a diagonal block is given by  $1/\sqrt{\frac{8n^j}{n_j-1} \left(1 - \frac{2n^j}{n_j(n_j-1)}\right)}$ , and  $1/\sqrt{\frac{4n^{jk}}{\sqrt{n_j n_k}} \left(1 - \frac{n^{jk}}{n_j n_k}\right)}$  for an off-diagonal block, where  $n^j$  denotes the total number of edges in the  $j$ -th diagonal block  $A_{n_j \times n_j}^j$ , and  $n^{jk}$  denotes the total number of edges in the off-diagonal block  $B_{n_j \times n_k}^{j,k}$ . In our study, the quantity  $(n^j)$  depends on the threshold distance (Td) between the residues within a single diagonal block, representing intra-layer connections. In contrast,  $(n^{jk})$  is determined by the threshold distance ( $\text{Td}_{\text{Inter}}$ ), which characterizes the interaction between residues from two different diagonal blocks, corresponding to inter-layer connections.

This study explores how the threshold distance influences the connectivity in protein crystal structure. Two approaches are considered for varying the threshold distance. In the first approach, the intra-layer and inter-layer threshold distances, denoted as Td and  $\text{Td}_{\text{Inter}}$ , are taken to be the same and are increased simultaneously in a parallel manner. This allows us to observe the evolution of the network under uniform enhancement of connectivity. In the second approach, we fix the intra-layer threshold distance within each diagonal block and increase the inter-layer threshold distance  $\text{Td}_{\text{Inter}}$  independently, thereby selectively enhancing inter-monomer connections. These two methods provide insight into how different connectivity modes influence the emergent structural properties and the potential transition between universal regimes in these networks.

First, we analyze the protein structure 1EWT, in which each monomer has 456 residues. As a result, the corresponding adjacency matrix  $\mathcal{A}$  is of dimension  $912 \times 912$ , each diagonal block representing intra-monomer interactions is of size  $456 \times 456$ , and the off-diagonal blocks, corresponding to inter-monomer interactions, are also of size  $456 \times 456$ . Following the first approach, for a threshold distance of  $\text{Td} = \text{Td}_{\text{Inter}} = 5.5 \text{ \AA}$ , block one contains 915 connections and block two contains 911 connections, with no inter-layer connections. Increasing  $\text{Td} = \text{Td}_{\text{Inter}} = 5.5$  to  $6 \text{ \AA}$  introduces the first inter-

layer connection, meanwhile the intra-layer complexity increases, yielding 1250 and 1248 connections in block one and block two, respectively. At  $\text{Td} = \text{Td}_{\text{Inter}} = 7 \text{ \AA}$ , four inter-layer connections emerge, and the intra-layer connections increase to 1817 and 1826. At this point, the second-order ( $k = 2$ ) SRD and CSRSD statistics align well with  $\alpha = 2$ , as shown in Fig. 11(a) and Fig. 12(a). Further increasing the threshold distance to  $\text{Td} = \text{Td}_{\text{Inter}} = 8 \text{ \AA}$  results in 22 inter-layer connections, with 2284 and 2274 intra-layer connections in the two blocks. The spectral statistics remains consistent with  $\alpha = 2$ , as seen in Fig. 11(b) and Fig. 12(b). When  $\text{Td} = \text{Td}_{\text{Inter}}$  is raised to  $9 \text{ \AA}$ , 37 inter-layer connections are observed, and the intra-layer connections grow to 3073 and 3052 in blocks one and two, respectively. The corresponding SRD and CSRSD statistics exhibit a transition toward an intermediate regime between  $\alpha = 2$  and  $\alpha = 4$ , as shown in Fig. 11(c) and Fig. 12(c). At  $\text{Td} = \text{Td}_{\text{Inter}} = 10 \text{ \AA}$ , the number of inter-layer connections increases to 75, with blocks one and two containing 4225 and 4227 intra-layer connections, respectively. The statistics still exhibit an intermediate regime between  $\alpha = 2$  and  $\alpha = 4$ , as shown in Fig. 11(d) and Fig. 12(d). At  $\text{Td} = \text{Td}_{\text{Inter}} = 11 \text{ \AA}$ , the number of inter-layer connections increases to 147, with block one and block two containing 5621 and 5597 intra-layer connections, respectively. In this case, the spectral statistics lie close to  $\alpha = 4$ , as demonstrated in Fig. 11(e) and Fig. 12(e).

In the second approach to analyze the crossover behaviour, we fixed the intra-layer threshold distance at  $\text{Td} = 7 \text{ \AA}$ . we varied the inter-layer threshold distance  $\text{Td}_{\text{Inter}}$  from  $6 \text{ \AA}$  to  $11 \text{ \AA}$ . This results in a continuous crossover in the SRD and CSRSD statistics, evolving from  $\alpha = 2$  to  $\alpha = 4$ , as shown in Figs. 11(f)–(j) and 12(f)–(j). These observations highlight the sensitivity of spectral behaviour to the coupling structure and demonstrate how increasing inter-layer connectivity induces a transition between different universality classes.

Next, we analyze the bilayer structure of the 1EWK protein, where one monomer contains 449 residues and the other contains 450 residues. Consequently, the diagonal blocks of the adjacency matrix  $\mathcal{A}$  have dimensions  $449 \times 449$  and  $450 \times 450$  respectively, yielding a total matrix dimension of  $899 \times 899$ . The upper off-diagonal block, representing inter-layer connections, has dimensions  $449 \times 450$ . In this configuration, for the first approach, we perform the analysis by increasing both threshold parameters, Td and  $\text{Td}_{\text{Inter}}$ , simultaneously for  $k = 2$  and  $k = 3$ . At an initial threshold distance of  $\text{Td} = \text{Td}_{\text{Inter}} = 5.5 \text{ \AA}$ , block one contains 931 connections, block two has 929 connections, and no inter-layer connections are observed. Increasing the threshold to  $\text{Td} = \text{Td}_{\text{Inter}} = 6 \text{ \AA}$ , five inter-layer connections emerge, while intra-layer complexity increases, with block one and block two containing 1246 and 1244 connections, respectively. At  $\text{Td} = \text{Td}_{\text{Inter}} = 7 \text{ \AA}$ , 18 inter-layer connections are observed, with 1799 and 1802 intra-layer connections in blocks one and two, respec-

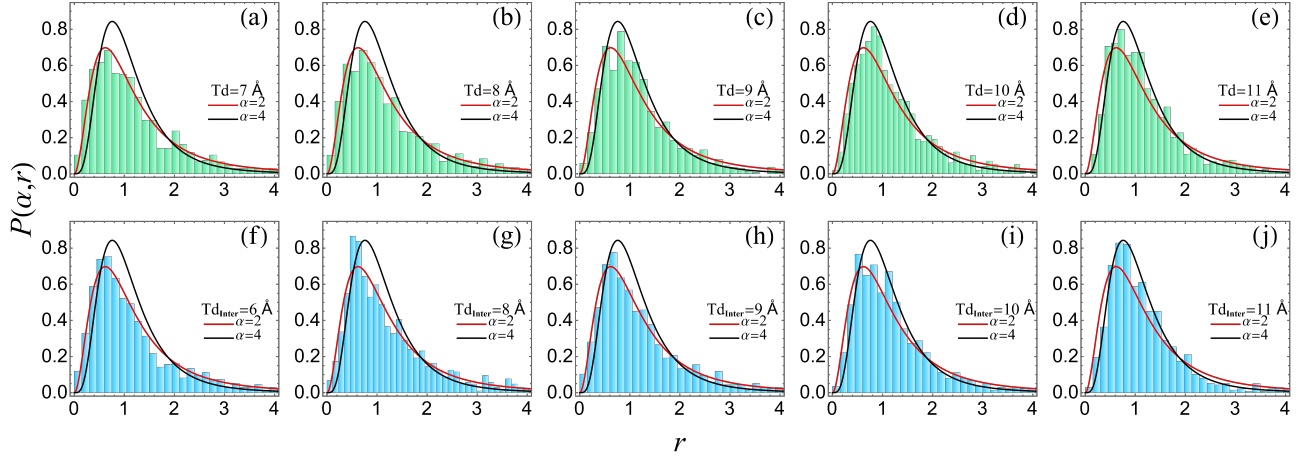


FIG. 11. Second-order ( $k = 2$ ) SRD plots (histogram) are presented for the bilayer 1EWT protein crystal structure ( $m = 2$ ), where each diagonal block of the adjacency matrix  $\mathcal{A}$  has dimensions  $456 \times 456$ . The histograms correspond to different combinations of intra-layer and inter-layer threshold distances ( $T_d$  and  $T_{d_{\text{Inter}}}$ ) in Å, along with the number of intra-layer edges in block one ( $n^1$ ), block two ( $n^2$ ), and the number of inter-layer edges ( $n^{12}$ ). The SRD plots are obtained for the following cases ( $T_d, T_{d_{\text{Inter}}}, n^1, n^2, n^{12}$ ): (a) (7, 7, 1817, 1826, 4), (b) (8, 8, 2284, 2274, 22), (c) (9, 9, 3073, 3052, 37), (d) (10, 10, 4225, 4227, 75), (e) (11, 11, 5621, 5597, 147), (f) (7, 6, 1250, 1248, 1), (g) (7, 8, 1817, 1826, 22), (h) (7, 9, 1817, 1826, 37), (i) (7, 10, 1817, 1826, 75), and (j) (7, 11, 1817, 1826, 147).

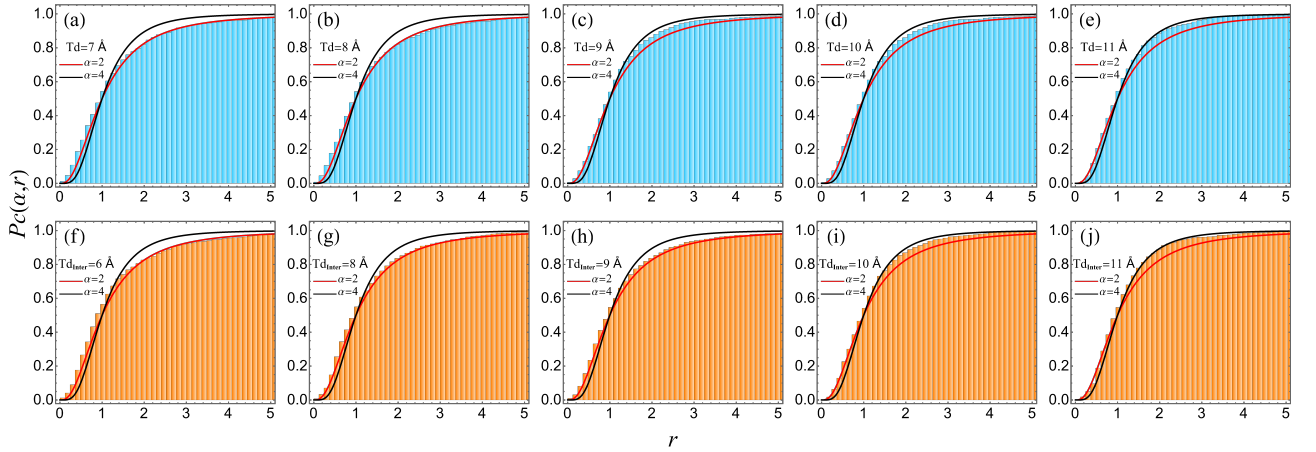


FIG. 12. Second order ( $k = 2$ ) CSRD plots (histogram), The parameter values used as Fig. 11.

tively. At this threshold, the statistics of the second-order ( $k = 2$ ) SRD and CSRD align well with  $\alpha = 2$ , as shown in Fig. 13(a) and Fig. 14(a). Further increasing the threshold to  $T_d = T_{d_{\text{Inter}}} = 8$  Å leads to a rise in inter-layer connections, with block one containing 2267 and block two containing 2248 intra-layer connections. The SRD and CSRD statistics remains close to  $\alpha = 2$  result, as shown in Fig. 13(b) and Fig. 14(b). At  $T_d = T_{d_{\text{Inter}}} = 9$  Å, 52 inter-layer connections emerge, and intra-layer connections increase to 3058 and 3041 in the respective blocks. For  $k = 2$ , SRD and CSRD statistics shift to an intermediate regime between  $\alpha = 2$  and  $\alpha = 4$ , as illustrated in Figs. 13(c) and 14(c). At  $T_d = T_{d_{\text{Inter}}} = 10$  Å, the number of inter-layer edges rises to 95, with intra-layer edges totaling 4122 and 4167, and the statistics continue to exhibit intermediate be-

havior between  $\alpha = 2$  and  $\alpha = 4$ , as seen in Figs. 13(d) and 14(d). Finally, at  $T_d = T_{d_{\text{Inter}}} = 11$  Å, 171 inter-layer connections are observed, and the intra-layer edges increase to 5668 and 5601. In this case, the SRD and CSRD statistics for  $k = 2$  closely follow the distribution associated with  $\alpha = 4$ , as shown in Figs. 13(e) and 14(e). Additionally, for the third-order ( $k = 3$ ) case, the SRD and CSRD statistics display a continuous crossover from  $\alpha = 4$  to  $\alpha = 8$ , as illustrated in Figs. 13(f)–(j) and 14(f)–(j).

In a second approach, we fixed the threshold distance within the diagonal blocks while varying the threshold distance exclusively for the off-diagonal blocks. This method yielded similar statistical behaviour, revealing a continuous crossover in the SRD and CSRD statistics. for  $k = 2$ , the statistics evolved from  $\alpha = 2$  to  $\alpha = 4$  and



$k = 3$ , the statistics evolved from  $\alpha = 4$  to  $\alpha = 8$ , indicating a gradual transition in the underlying structural correlations.

Finally, in the structure 1UW6, five monomers assemble to form a pentameric unit. Subsequently, four such pentameric units are further organized into a higher-order quaternary structure, resulting in a 20-subunit capsid-like assembly. In this protein crystal structure, we consider 4134 residues involved in interactions, resulting in an adjacency matrix  $\mathcal{A}$  of dimensions  $4134 \times 4134$ . The residues are divided into four block structures, with blocks one and two containing 1033 residues each, and blocks three and four containing 1034 residues each. Initially, in the first approach, at a threshold distance  $Td = Td_{\text{Inter}} = 5 \text{ \AA}$ , the number of edges in blocks one, two, three, and four are 1349, 1350, 1352, and 1348, respectively, with a single inter-layer connection between blocks one and two. At  $Td = Td_{\text{Inter}} = 5.5 \text{ \AA}$ , the number of edges increases to 1852, 1862, 1873, and 1888 in blocks one through four, respectively, with two inter-layer connections: one between blocks one and two, and another between blocks two and four. The second-order ( $k = 2$ ) SRD and CSRD statistics align with  $\alpha = 1$ , as shown in Fig. 15(a) and Fig. 16(a), indicating the presence of a well-defined four-block network structure, in agreement with Table I. As the threshold distance increases to  $Td = Td_{\text{Inter}} = 6 \text{ \AA}$ , the edge count grows to 2651, 2645, 2656, and 2663 in the respective blocks, with four inter-layer connections: one between blocks one and two, and three between blocks two and four. The SRD and CSRD statistics continue to exhibit agreement with  $\alpha = 1$  (Fig. 15(b) and Fig. 16(b)). At  $Td = Td_{\text{Inter}} = 7 \text{ \AA}$ , the number of edges rise to 4101, 4111, 4014, and 4086, respectively. Nine inter-layer connections are observed—five between blocks one and two, and four between blocks two and four resulting in SRD and CSRD statistics that shows intermediate behavior between  $\alpha = 1$  and  $\alpha = 2$  (Fig. 15(c) and Fig. 16(c)). When the threshold is increased to  $Td = Td_{\text{Inter}} = 8 \text{ \AA}$ , there are 5187, 5174, 5370, and 5190 intra-layer connections respectively with 29 inter-layer connections (13 between blocks one and two, and 16 between blocks two and four). At  $Td = Td_{\text{Inter}} = 9 \text{ \AA}$ , the intra-layer edge counts increase to 6932, 6931, 6933, and 6950 respectively, with 64 inter-layer connections (25 between blocks one and two, and 39 between blocks two and four), the SRD and CSRD statistics remains intermediate between  $\alpha = 1$  and  $\alpha = 2$  (Fig. 15(d) and Fig. 16(d)). Finally, at  $Td = Td_{\text{Inter}} = 10 \text{ \AA}$ , the number of intra-layer connections reach 9632, 9602, 9630, and 9618 respectively, with 138 inter-layer connections (58 between blocks one and two, and 70 between blocks two and four), while block three remains isolated. At this stage, the second-order ( $k = 2$ ) SRD and CSRD statistics transitions fully to  $\alpha = 2$ , indicating that the original four-block structure has effectively merged into a two-block system, with blocks one, two, and four forming a single block through inter-layer interaction and while block three re-

mains uncoupled (Fig. 15(e) and Fig. 16(e)). Implementing the second approach to analyze crossover behaviour, the intra-layer threshold distance is fixed at  $Td = 6 \text{ \AA}$ , while the inter-layer threshold distance  $Td_{\text{Inter}}$  is varied independently from  $5.5 \text{ \AA}$  to  $10 \text{ \AA}$ . This analysis reveals a continuous crossover in the SRD and CSRD statistics, evolving from  $\alpha = 4$  to  $\alpha = 2$ , as shown in Figs. 15(f)–(j) and 16(f)–(j), reflecting how variations in inter-layer connectivity govern spectral transitions.

## V. SUMMARY AND CONCLUSION

In this work, we investigated higher-order spectral fluctuations in multilayer networks through the lens of RMT, with an emphasis on identification of universal spectral properties. By analyzing adjacency matrix spectra under various configurations, including networks with solely intra-layer or inter-layer connections, multiplex networks, and those combining both, we demonstrated that spectral fluctuations align with RMT predictions when adjacency matrices are properly scaled. These results reveal the emergence of universality in multilayer network spectra across diverse topologies and connection probabilities.

Additionally, we introduced a crossover model to characterize the transition in spectral statistics of bilayer networks as the relative inter-layer and intra-layer connection strength parameter  $\gamma$  is varied. The results highlight a transition from block diagonal statistics (two independent GOEs) to single-layer statistics (single GOE), depending on network size and  $\gamma$  while illustrating tunable spectral behavior.

Furthermore, we applied these insights to the analysis of protein crystal structures (1EWT, 1EWK, and 1UW6) by setting a threshold on interatomic distances to define connections, and using SRD and CSRD as tools to analyze the complexity and universality of these systems. Protein crystal structures represent highly complex, spatially organized systems. Modeling these structures as multilayer interatomic distance networks provides insights into how threshold distances influence intra-layer and inter-layer connections, revealing transitions in network spectral properties. This crossover helps us to understand how proteins separate functional regions and develop modular structures, and how these features can be quantitatively analysed using random matrix theory. This approach offers a quantitative framework to systematically analyze and compare protein structures with potential applications in protein classification and drug design.

In conclusion, this study underscores the importance of RMT in understanding the universal fluctuation properties of multilayer networks, which serve as a powerful tool for elucidating the topological and dynamical complexities of various real-world systems. By applying these principles to interatomic distance networks in protein crystal structure, we have shown that spectral fluctuations can provide a deeper understanding of these

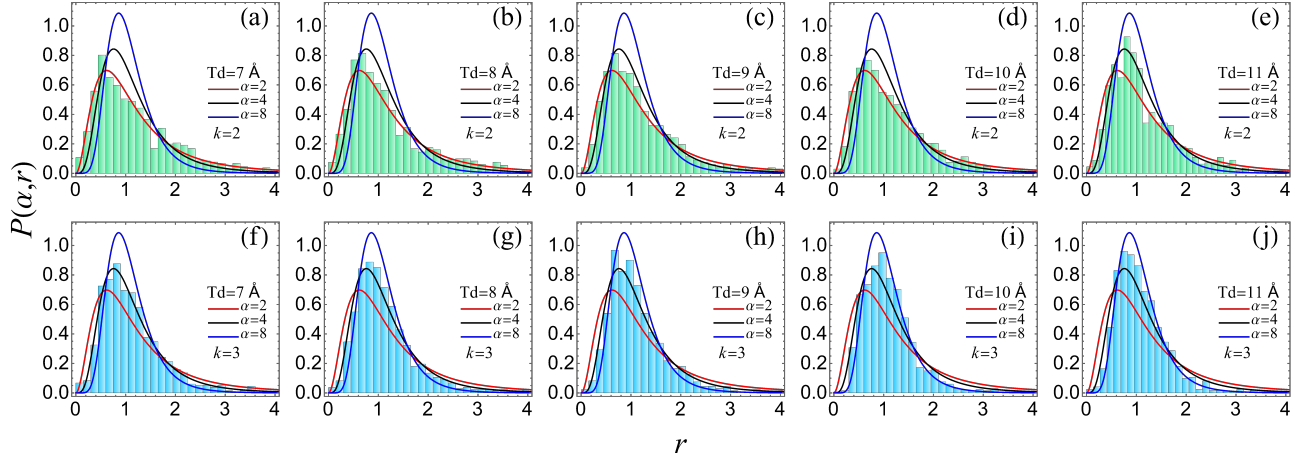


FIG. 13. Higher order SRD plots (histogram) are presented for the bilayer 1EWK protein crystal structure ( $m = 2$ ), where the diagonal blocks of the adjacency matrix  $\mathcal{A}$  have dimensions  $448 \times 448$  and  $447 \times 447$ , respectively. The histograms for second-order ( $k = 2$ ) and third-order ( $k = 3$ ) SRD correspond to different combinations of intra layer and inter layer threshold distances (Td and Td<sub>Inter</sub>) in Å, along with the number of intra layer edges in block one ( $n^1$ ), block two ( $n^2$ ), and the number of inter-layer edges ( $n^{12}$ ). The SRD plots are obtained for the following cases, denoted as  $(k, \text{Td}, \text{Td}_{\text{Inter}}, n^1, n^2, n^{12})$ : (a) (2,7,7,1799,1802,18), (b) (2,8,8,2267,2248,25), (c) (2,9,9,3058,3041,52), (d) (2,10,10,4122,4167,95), (e) (2,11,11,5668,5601,171), (f) (3,7,7,1799,1802,18), (g) (3,8,8,2267,2248,25), (h) (3,9,9,3058,3041,52), (i) (3,10,10,4122,4167,95), and (j) (3,11,11,5668,5601,171).

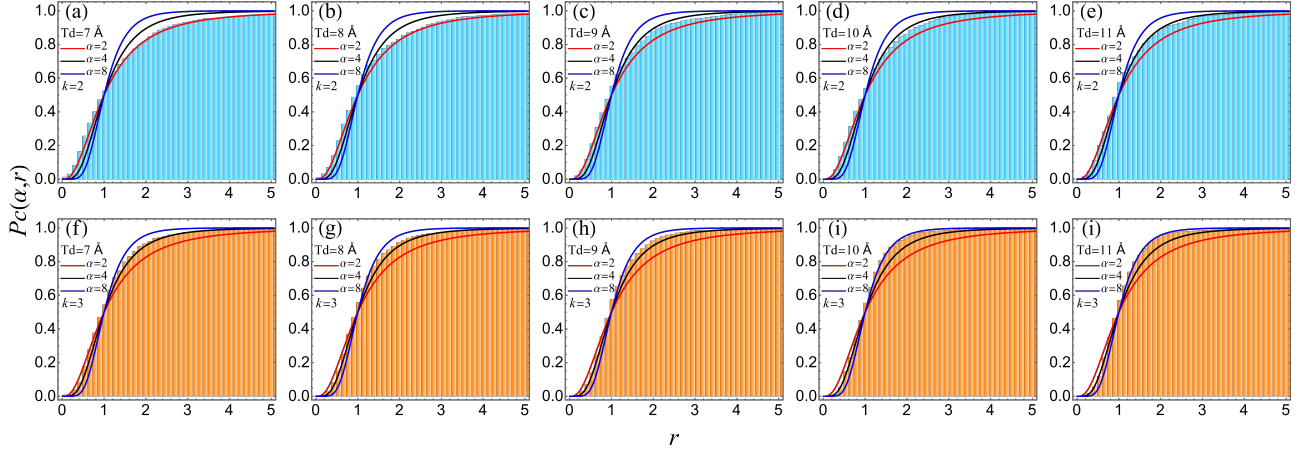


FIG. 14. Higher order of CSR plots (histogram), The parameter values used as Fig. 13.

biological systems underlying structural and functional characteristics.

## ACKNOWLEDGMENTS

H.S. and A.D. would like to thank Shiv Nadar Institution of Eminence for financial support.

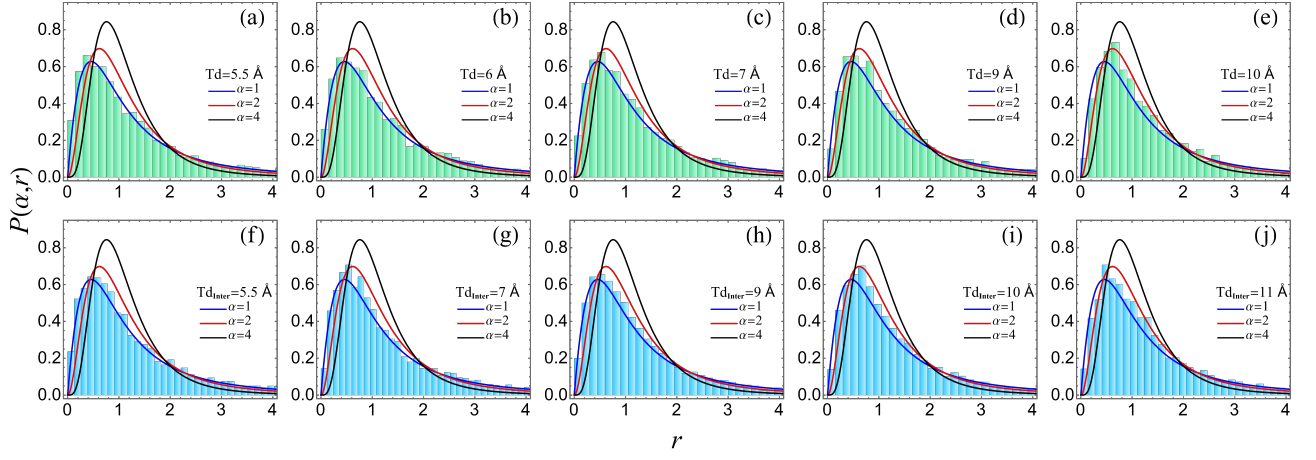


FIG. 15. Second-order ( $k = 2$ ) SRD plots (histogram) are presented for the tetralayer 1UW6 protein crystal structure ( $m = 4$ ). The diagonal blocks of the adjacency matrix  $\mathcal{A}$  correspond to dimensions  $1034 \times 1034$ ,  $1034 \times 1034$ ,  $1033 \times 1033$ , and  $1033 \times 1033$  for blocks one through four, respectively. The histograms represent various combinations of intra-layer and inter-layer threshold distances ( $T_d$ ,  $T_{d_{\text{inter}}}$ ) in Å, along with the number of intra-layer edges in block one ( $n^1$ ), block two ( $n^2$ ), block three ( $n^3$ ), block four ( $n^4$ ), and the number of inter-layer edges between block pairs: one and two ( $n^{12}$ ), one and three ( $n^{13}$ ), one and four ( $n^{14}$ ), two and three ( $n^{23}$ ), two and four ( $n^{24}$ ), and three and four ( $n^{34}$ ). The SRD plots are obtained for the following parameter sets: (a) (5.5, 5.5, 1852, 1862, 1873, 1888, 1, 0, 0, 0, 1, 0), (b) (6, 6, 2651, 2645, 2656, 2663, 1, 0, 0, 0, 3, 0), (c) (7, 7, 4101, 4111, 4094, 4086, 5, 0, 0, 0, 4, 0), (d) (9, 9, 6932, 6931, 6933, 6950, 25, 0, 0, 0, 39, 0), (e) (10, 10, 9632, 9602, 9630, 9618, 58, 0, 0, 0, 70, 0), (f) (5.5, 6, 1852, 1862, 1873, 1888, 1, 0, 0, 1, 0), (g) (5.5, 7, 1852, 1862, 1873, 1888, 5, 0, 0, 0, 4, 0), (h) (5.5, 9, 1852, 1862, 1873, 1888, 25, 0, 0, 0, 39, 0), (i) (5.5, 10, 1852, 1862, 1873, 1888, 1817, 1826, 58, 0, 0, 70), and (j) (5.5, 11, 1852, 1862, 1873, 1888, 1817, 95, 0, 0, 0, 113).

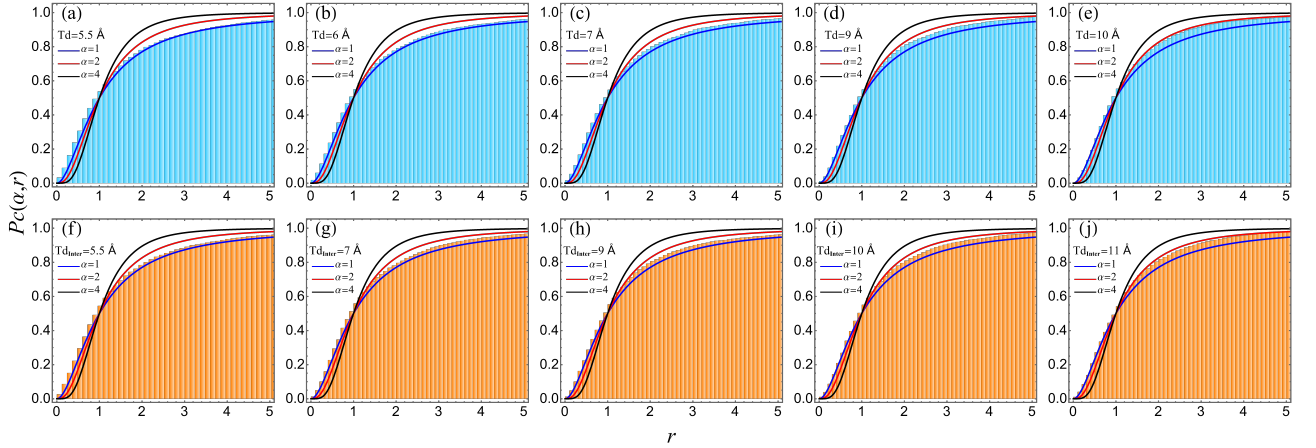


FIG. 16. Second order ( $k = 2$ ) CSRD plots (histogram), The parameter values used as Fig. 15

### Appendix A: Closed-form expressions for cumulative spacing ratio distribution

The cumulative spacing ratio distribution (CSRD) is defined as

$$\begin{aligned} P_c(\alpha, r) &= \int_0^r P(\alpha, r) dr \\ &= \int_0^r C_\alpha \frac{(r + r^2)^\alpha}{(1 + r + r^2)^{1+3\alpha/2}} dr. \end{aligned} \quad (\text{A1})$$

Here we provide explicit closed-form expressions for CSRD for different  $\alpha$  values used in this work.

For  $\alpha = 1$ :

$$P_c(\alpha = 1, r) = \frac{1}{4} \left( 2 + \frac{(1 + 2s)(-2 + s + s^2)}{(1 + s + s^2)^{3/2}} \right), \quad (\text{A2})$$

$\alpha = 2$ :

$$P_c(\alpha = 2, r) = -\frac{1}{2} + \frac{3\sqrt{3}(-1+s)s(1+s)(2+s)(1+2s)}{4\pi(1+s+s^2)^3} + \frac{3 \arctan\left(\frac{1+2s}{\sqrt{3}}\right)}{\pi} \quad (\text{A3})$$

$\alpha = 4$ :

$$P_c(\alpha = 4, r) = -\frac{1}{2} + \frac{3\sqrt{3}(-1+s)s(1+s)(2+s)(1+2s)(2+s(1+s)(6+s(1+s)(15+2s(1+s))))}{8\pi(1+s+s^2)^6} + \frac{3 \arctan\left(\frac{1+2s}{\sqrt{3}}\right)}{\pi} \quad (\text{A4})$$

$\alpha = 8$ :

$$P_c(\alpha = 8, r) = -\frac{1}{2} + \frac{3\sqrt{3}(-1+s)s(1+s)(2+s)(1+2s)}{560\pi(1+s+s^2)^{12}} \times (140 + s(1+s)(1260 + s(1+s)(5670 + s(1+s)(15540 + s(1+s)(30492 + s(1+s)(40446 + s(1+s)(51099 + 14s(1+s)(873 + 5s(1+s)(27 + 2s(1+s)))))))))) + \frac{3 \arctan\left(\frac{1+2s}{\sqrt{3}}\right)}{\pi} \quad (\text{A5})$$

- 
- [1] A.-L. Barabási, *Linked: The New Science of Networks* (East-Asia Publishing Company, 2002).
  - [2] M. Newman, *Networks* (Oxford University Press, 2018).
  - [3] S. H. Strogatz, *Exploring complex networks*, Nature 410, 268–276 (2001).
  - [4] S. Boccaletti, V. Latora, Y. Moreno, M. Chavez, and D. U. Hwang, *Complex networks: Structure and dynamics*, Phys. Rep. 424, 175–308 (2006).
  - [5] E. Estrada, *The Structure of Complex Network: Theory and Applications* (ACS, 2012).
  - [6] L. Euler, *Solutio problematis ad geometriam situs pertinentis*, *Commentarii academiae scientiarum Petropolitanae*, 128 (1741).
  - [7] S. Wasserman and K. Faust, *Social network analysis - methods and applications*, (1994).
  - [8] J. M. Larson, *Networks of conflict and cooperation*, Annual Review of Political Science 24, 89 (2021).
  - [9] D. A. Luke and J. K. Harris, *Network analysis in public health: history, methods, and applications*, Annual review of public health 28, 69 (2007).
  - [10] A.-L. Barabási, N. Gulbahce, and J. Loscalzo, *Network medicine: a network-based approach to human disease*, Nature reviews genetics 12, 56 (2011).
  - [11] M. D. Jackson, S. Duran-Nebreda, and G. W. Bassel, *Network-based approaches to quantify multicellular development*, Journal of The Royal Society Interface 14, 20170484 (2017).
  - [12] F. Emmert-Streib, S. Tripathi, O. P. Yli-Harja, and M. Dehmer, *Understanding the world economy in terms of networks: A survey of data-based network science approaches on economic networks*, Frontiers Appl. Math. Stat. 4, 37 (2018).
  - [13] R. Cohen, K. Erez, D. Avraham and S. Havlin, *Resilience of the Internet to Random Breakdowns*, Phys. Rev. Lett. 85, 4626 (2000).
  - [14] A.-L. Barabási, H. Jeong, Z. Neda, E. Ravasz, A. Schubert, and T. Vicsek, *Evolution of the social network of scientific collaborations*, Physica A: Statistical mechanics and its applications 311, 590 (2002).
  - [15] M. Barthélemy, *Spatial networks*, Physics reports 499, 1 (2011).
  - [16] P. Erdős and A. Rényi, *On random graphs I.*, (1960).
  - [17] B. Bollobás, *Random graphs*, in *Modern graph theory* (Springer, 1998) pp. 215–252.
  - [18] E. N. Gilbert, *Random graphs*, The Annals of Mathematical Statistics 30, 1141 (1959).
  - [19] S. E. Fienberg, *A brief history of statistical models for network analysis and open challenges*, Journal of Computational and Graphical Statistics 21, 825 (2012).
  - [20] D. J. Watts and S. H. Strogatz, *Collective dynamics of ‘small-world’ networks*, Nature 393, 440 (1998).
  - [21] R. Albert and A.-L. Barabási, *Statistical mechanics of complex networks*, Reviews of modern physics 74, 47 (2002).
  - [22] J. N. Bandyopadhyay and S. Jalan, *Universality in complex networks: Random matrix analysis*, Physical Review E 76, 026109 (2007).
  - [23] S. Jalan and J. N. Bandyopadhyay, *Random matrix analysis of complex networks*, Physical Review E 76, 046107 (2007).
  - [24] A. Rai, A. V. Menon, and S. Jalan, *Randomness and preserved patterns in cancer network*, Sci. Rep. 4, 6368 (2014).
  - [25] M. Kothiyal, S. Kumar, and N. Sukumar, *Investigation of chemical space networks using graph measures and random matrix theory*, J. Math. Chem. 60, 891 (2022).

- [26] A. Wei, W. Hu, and J. Steinhardt, More than a toy: Random matrix models predict how real-world neural representations generalize, *Proceedings of the International Conference on Machine Learning* (PMLR, 2022), pp. 23549-23588.
- [27] R. Wang, L. Wang, Y. Yang, J. Li, Y. Wu, and P. Lin, Random matrix theory for analyzing the brain functional network in attention deficit hyperactivity disorder, *Phys. Rev. E* 94, 052411 (2016).
- [28] M. Kivelä, A. Arenas, M. Barthélemy, J. P. Gleeson, Y. Moreno, and M. A. Porter, Multilayer networks, *Journal of complex networks* 2, 203 (2014).
- [29] S. Boccaletti, G. Bianconi, R. Criado, C. I. Del Genio, J. Gómez-Gardenes, M. Romance, I. Sendina-Nadal, Z. Wang, and M. Zanin, The structure and dynamics of multilayer networks, *Physics reports* 544, 1 (2014).
- [30] M. De Domenico, A. Solé-Ribalta, E. Cozzo, M. Kivelä, Y. Moreno, M. A. Porter, S. Gómez, and A. Arenas, Mathematical formulation of multilayer networks, *Physical Review X* 3, 041022 (2013).
- [31] E. Cozzo, G. F. d. Arruda, F. A. Rodrigues, and Y. Moreno, Multilayer networks: metrics and spectral properties, in *Interconnected networks* (Springer, 2016) pp. 17-35.
- [32] M. De Domenico, C. Granell, M. A. Porter, and A. Arenas, The physics of spreading processes in multilayer networks, *Nat. Phys.* 12, 901–906 (2016).
- [33] T. Raghav and S. Jalan, Random matrix analysis of multiplex networks, *Physica A: Statistical Mechanics and its Applications* 586, 126457 (2022).
- [34] T. Raghav and S. Jalan, Spacing ratio statistics of multiplex directed networks. *New Journal of Physics*, 25, 053012, (2023).
- [35] G. Tapia-Labra, M. Hernández-Sánchez, J. A. Méndez-Bermúdez, Multilayer directed random networks: Scaling of spectral properties, *Chaos, Solitons and Fractals*, 199, 116695 (2025)
- [36] V. Oganesyan and D. A. Huse, Localization of interacting fermions at high temperature, *Phys. Rev. B* 75, 155111 (2007).
- [37] Y. Y. Atas, E. Bogomolny, O. Giraud, and G. Roux, Distribution of the ratio of consecutive level spacings in random matrix ensembles, *Phys. Rev. Lett.* 110, 084101 (2013).
- [38] M. L. Mehta, *Random Matrices*, 3rd Ed. (Academic, New York, 2004).
- [39] U. T. Bhosale, Superposition and higher-order spacing ratios in random matrix theory with application to complex systems, *Phys. Rev. B* 104, 054204 (2021).
- [40] O. Giraud, N. Macé, É. Vernier and F. Alet, Probing Symmetries of Quantum Many-Body Systems through Gap Ratio Statistics, *Phys. Rev. X* 12, 011006 (2022).
- [41] A. Mishra and K. H. Cheong, Exploring universality of the  $\beta$ -Gaussian ensemble in complex networks via intermediate eigenvalue statistics, *Phys. Rev. E* 109, 014218 (2024).
- [42] S. H. Tekur, U. T. Bhosale, and M. S. Santhanam, Higher-order spacing ratios in random matrix theory and complex quantum systems, *Phys. Rev. B* 98, 104305 (2018).
- [43] U. T. Bhosale, S. H. Tekur, and M. S. Santhanam, Scaling in the eigenvalue fluctuations of correlation matrices, *Phys. Rev. E* 98, 052133 (2018).
- [44] I. J. Farkas, I. Derényi, A.-L. Barabási, and T. Vicsek, *Phys. Rev. E* 64, 026704 (2001).
- [45] Y. Zhao, *Spectral Distributions of Random Graphs*, Technical Report, MIT (2012).
- [46] C. Sarkar and S. Jalan, Social patterns revealed through random matrix theory, *Europhys. Lett.* 108, 48003 (2014).
- [47] J. M. Buldú and M. A. Porter, Frequency-based brain networks: From a multiplex framework to a full multilayer description, *Netw. Neurosci.* 2, 418–441 (2018).
- [48] Z. Hammoud and F. Kramer, *Big Data Analytics* 5, 2 (2020).
- [49] B. L. Goldblum, A. W. Reddie, T. C. Hickey, J. E. Bevens, S. Laderman, N. Mahowald, A. P. Wright, E. Katzenson, and Y. Mubarak, *Appl. Netw. Sci.* 4, 1 (2019).
- [50] A. Aleta and Moreno, Multilayer networks in a nutshell, *Annual Review of Condensed Matter Physics*, 10(1) 45-62 (2019).
- [51] A. Agrawal, C. Sarkar, S. K. Dwivedi, N. Dhasmana, and S. Jalan, Quantifying randomness in protein-protein interaction networks of different species: A random matrix approach, *Physica A* 404, 359 (2014).
- [52] R. Potestio, F. Caccioli, and P. Vivo, Random Matrix Approach to Collective Behavior and Bulk Universality in Protein Dynamics, *Phys. Rev. Lett.* 103, 268101 (2009).
- [53] A. Zhang, *Protein Interaction Networks: Computational Analysis* (Cambridge University Press, 2009).